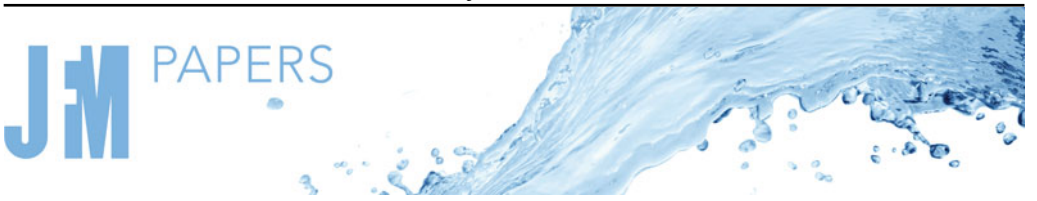
J. Fluid Mech. (2026), *vol.* 1043, A13, doi:10.1017/jfm.2026.11943



Quantitatively mapping the Eady model onto a two-layer quasi-geostrophic model

Julie Meunier[1] **and Basile Gallet**[1]

[1]CNRS, CEA, Service de Physique de l'Etat Condensé, Université Paris-Saclay, Gif-sur-Yvette 91191, France

Corresponding author: Julie Meunier, jmem4@cam.ac.uk

(Received 24 October 2025 UTC; revised 9 July 2026 UTC; accepted 15 July 2026 UTC)

The two-layer quasi-geostrophic (2LQG) model and the Eady model are two idealised systems illustrating the baroclinic instability of atmospheric jets and ocean currents. The two set-ups share many ingredients – background vertically sheared zonal flow of density-stratified fluid in a rapidly rotating frame – while differing in complexity and dimensionality. The Eady model has a continuous vertical direction, with baroclinic turbulence induced by boundary potential vorticity (PV) gradients at top and bottom. By contrast, the 2LQG sytem typically models baroclinic instability induced by interior PV gradients. This distinction challenges our ability to clearly identify a couple of 'modes' through which the Eady dynamics could be inferred from a simpler 2LQG system. In the present study, we show that this difficulty can be circumvented in the turbulent regime arising for weak bottom drag. Namely, guided by the common organisation of both systems into a gas of coherent vortices, we identify a quantitative mapping between the Eady and 2LQG models. The mapping allows for parameter-free predictions of the eddy diffusivity of the Eady model based on knowledge of the 2LQG diffusivity. We illustrate these results using numerical simulations of the Eady and 2LQG models with linear or quadratic bottom drag.

Key words: baroclinic flows, vortex dynamics, quasi-geostrophic flows

1. Introduction

In rapidly rotating density-stratified fluids, large-scale vertically sheared zonal flows are in thermal-wind balance with a lateral buoyancy gradient. This configuration, common to both ocean currents and atmospheric jets, is prone to baroclinic instability, and results in a turbulent flow. To model this phenomenon and assess the effective transport properties of such 'baroclinic turbulence', one typically resorts to idealised models that retain only the

© The Author(s), 2026. Published by Cambridge University Press.

https://doi.org/10.1017/jfm.2026.11943 Published online by Cambridge University Press

key features of the system while avoiding unnecessary complexity. The two simplest such models are arguably the two-layer quasi-geostrophic (2LQG) model and the Eady model. The 2LQG model involves two fluid layers of different density lying on top of one another, and the dynamics is described using two streamfunctions characterising the vertically invariant horizontal flow in each layer (Phillips 1954; Salmon 1978, 1980; Larichev & Held 1995; Arbic & Flierl 2004; Thompson & Young 2006; Kohl & O'Gorman 2022; Pudig & Smith 2025; Sterl *et al.* 2025; Lobo & Griffies 2026). The governing equations of the 2LQG model are thus effectively two-dimensional (2-D). In contrast with the 2LQG model, the Boussinesq Eady model possesses a continuous vertical direction. All fields are functions of the three spatial coordinates, and time (Eady 1949). In the rapidly rotating limit, however, quasi-geostrophy (QG) allows for a crucial simplification. The potential vorticity (PV) vanishes in the interior of the domain, the consequence being that the dynamics reduce to 2-D evolution equations for the streamfunctions at the top and bottom of the domain.

Even in the simplest f-plane configuration considered in the present study, there are some crucial distinctions between the Eady and 2LQG models. The Eady model is driven by boundary PV gradients at top and bottom, while the 2LQG model possesses interior PV gradients. This leads to different phenomenologies for the two models at horizontal scales much smaller than the Rossby deformation radius: the Eady model exhibits the small-scale fronts and filamentary structures characteristic of surface quasi-geostrophy (SQG) (Constantin *et al.* 1994; Held *et al.* 1995; Capet *et al.* 2008; Scott & Dritschel 2014; Lapeyre 2017; Valade *et al.* 2025), whereas such structures are absent from the 2LQG model. From an analytical perspective, the distinction between boundary versus interior PV gradients leads to difficulties when attempting to isolate a unique set of vertical 'modes' through which the Eady model could be projected onto an equivalent 2LQG model. Among the various attempts are the early method proposed by Flierl (1978), the pedagogical approach of Vallis (2017), who crudely approximates the Eady model using finite differences with only two levels in the vertical, thereby obtaining a 2LQG model, and more general methods leading to non-unique bases of acceptable modes (Lapeyre 2009; Tulloch & Smith 2009; LaCasce 2012; Scott & Furnival 2012; Smith & Vanneste 2013; Yassin & Griffies 2022). Retaining only two modes from such a basis typically leads to a 2LQG model that disagrees quantitatively with the original Eady model (e.g. model A in Rocha *et al.* 2016), especially if the models are to be compared over a broad range of parameter values.

Despite these difficulties, however, the close mathematical structures of the Eady and 2LQG models suggest that a quantitative mapping between the two systems may be within reach. In the present study, we unveil such a mapping procedure by focusing on the low-drag regime. Besides showing that the large-scale dynamics of the two models are intimately connected, the mapping provides a way of quantitatively inferring the eddy diffusivity of the turbulent Eady model (among other quantities) based on the known behaviour of the simpler 2LQG model.

We introduce the Eady model and the 2LQG model in § 2. The first step of the mapping procedure consists of a reduction of the 2LQG equations to retain only the terms that contribute to the low-drag asymptotic behaviour. This task is carried out in § 3. The second step of the mapping procedure consists of a large-scale expansion of the Eady model, carried out in § 4. The expansion shows that up to a rescaling, both models are governed by the same asymptotic set of equations in the low-drag regime. As illustrated in § 5 for quadratic drag and in § 6 for linear drag, this allows for the quantitative and parameter-free prediction of the eddy diffusivity of the Eady model, based on existing scaling theories for the 2LQG diffusivity. We conclude in § 7.

https://doi.org/10.1017/jfm.2026.11943 Published online by Cambridge University Press

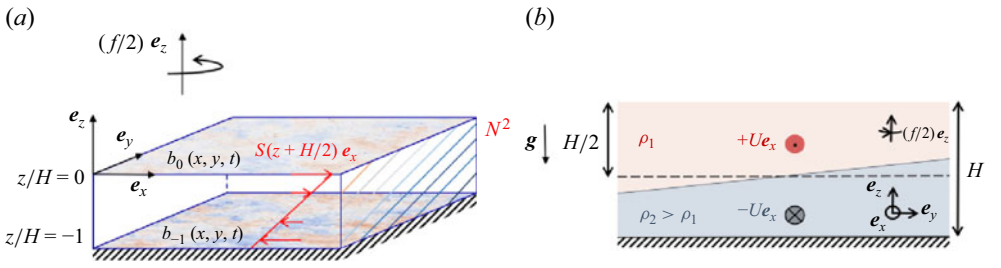


Figure 1. Two idealised models for the study of horizontally homogeneous baroclinic turbulence on the f-plane. (*a*) The Eady model features a continuous vertical direction z. (*b*) By contrast, the 2LQG model consists of two stacked shallow fluid layers. In both models, equilibrated turbulence results from a balance between potential energy release from the thermal-wind-balanced base state and dissipation by bottom drag.

2. The quasi-geostrophic Eady and two-layer models

2.1. *The Eady model*

The Eady model is sketched in figure 1(*a*). Consider a layer of fluid in a three-dimensional (3-D) domain $(x, y, z) \in [0, \mathcal{L}] \times [0, \mathcal{L}] \times [-H, 0]$, with weak density variations around a reference density ρ_0, described within the Boussinesq approximation. The fluid layer is subject to gravity $\boldsymbol{g}$ and rapid rotation at a rate $f/2$ around the vertical axis $\boldsymbol{e}_z$. The base state of the system consists of a vertically sheared zonal flow $\boldsymbol{U}(z) = S(z + H/2)\boldsymbol{e}_x$, with a uniform shear S. (We remove any uniform depth-invariant zonal flow by switching to the co-moving frame.) The density of the fluid is stably stratified along the vertical, with a uniform buoyancy frequency N. Because of thermal-wind balance, the vertically sheared flow $\boldsymbol{U}(z)$ implies the existence of a meridional buoyancy gradient $-fS$. That is, the background buoyancy field reads $B(y, z) = N^2 z - fSy$.

We consider departures from this base state obeying periodic boundary conditions in the horizontal directions. For small enough isopycnal slope fS/N^2, the evolution of the system is conveniently described within the QG approximation. The extensive derivation of the QG approximation for the present set-up is detailed in Gallet *et al.* (2022), and we only recall the main steps here. At lowest order in the QG expansion, the dominant flow satisfies geostrophic balance: the lowest-order flow is horizontal and divergence-free, with a streamfunction proportional to the departure pressure field. Hydrostatic balance indicates that the buoyancy departure is directly proportional to the vertical derivative of the departure pressure field. In particular, the dimensionless evolution equations for the buoyancy field at top and bottom read

$$\partial_t b_0 - \partial_x p_0 + \frac{1}{2}\partial_x b_0 + J(p_0, b_0) = 0, \tag{2.1}$$

$$\partial_t b_{-1} - \partial_x p_{-1} - \frac{1}{2}\partial_x b_{-1} + J(p_{-1}, b_{-1}) = \mu_{Eady}\boldsymbol{\nabla}\cdot(|\boldsymbol{\nabla} p_{-1}|\,\boldsymbol{\nabla} p_{-1}), \tag{2.2}$$

where $p_0(x, y, t)$ and $b_0(x, y, t)$ denote the dimensionless pressure and buoyancy departures at the top of the domain, while $p_{-1}(x, y, t)$ and $b_{-1}(x, y, t)$ denote the dimensionless pressure and buoyancy departures at the bottom of the domain. The horizontal advection terms are expressed using the Jacobian operator $J(g, h) = g_x h_y - g_y h_x$, and the friction term is written in compact form using the operator $\boldsymbol{\nabla} = (\partial_x, \partial_y)$.

In (2.1)–(2.2) and in the remainder of this subsection, we have non-dimensionalised time t with $N/(Sf)$, horizontal coordinates x and y with the Rossby deformation radius NH/f, vertical coordinate z with H, departure pressure with $\rho_0 H^2 SN$, and buoyancy with HSN.

https://doi.org/10.1017/jfm.2026.11943 Published online by Cambridge University Press

Strictly speaking, (2.2) corresponds to the evolution equation for buoyancy near the bottom of the domain, just above the small Ekman boundary layer. The right-hand-side term thus represents advection of the background stratification by the vertical velocity arising from Ekman pumping inside the boundary layer. We consider a stress on the rough ocean floor that is quadratic in outer flow velocity. The resulting pumping velocity is proportional to the curl of this quadratic stress, hence the right-hand-side term in (2.2), where μ_{Eady} denotes the dimensionless quadratic drag coefficient.

In the interior of the domain, the QG approximation naturally leads to material conservation of the quasi-geostrophic potential vorticity (QGPV). Because this equation has no source terms in the present context, one can focus on the vanishing QGPV state. Demanding that the QGPV be zero inside the domain readily provides a relation between the pressure at top and bottom, and its vertical derivative (i.e. the buoyancy) at top and bottom; see Gallet *et al.* (2022). The resulting inversion relation is more conveniently expressed in spectral space, relating the boundary values of buoyancy and pressure (or streamfunction) for each horizontal wavevector $\boldsymbol{k}$:

$$\begin{pmatrix} \hat{b}_0|_{\boldsymbol{k}} \\ \hat{b}_{-1}|_{\boldsymbol{k}} \end{pmatrix} = \begin{bmatrix} \dfrac{k}{\tanh(k)} & -\dfrac{k}{\sinh(k)} \\ \dfrac{k}{\sinh(k)} & -\dfrac{k}{\tanh(k)} \end{bmatrix} \begin{pmatrix} \hat{p}_0|_{\boldsymbol{k}} \\ \hat{p}_{-1}|_{\boldsymbol{k}} \end{pmatrix}, \tag{2.3}$$

where $\hat{\phi}|_{\boldsymbol{k}}$ denotes the Fourier coefficient of the field ϕ, and the horizontal wavevector $\boldsymbol{k}$ is non-dimensionalised using the Rossby deformation radius NH/f.

The QG Eady system consists of (2.1)–(2.2) with the inversion relation (2.3). We are interested in the long-time statistics of solutions to this system in a doubly periodic domain $(x,\, y) \in [0,\, L]^2$, with large-enough dimensionless domain size $L = \mathcal{L} f/(NH)$ for these statistics to be independent of L. A central quantity of interest is the meridional buoyancy flux induced by the turbulent flow in statistically steady state. One easily shows that this buoyancy flux is depth-independent for the present vanishing-PV states (Gallet *et al.* 2022; Meunier *et al.* 2023*b*). The time- and volume-averaged buoyancy flux is thus readily obtained from the time and horizontal-area average of the meridional buoyancy flux evaluated at the top or at the bottom of the domain. Denoting as D_{Eady} the buoyancy flux non-dimensionalised with $NH^2 S/f$, we simply obtain

$$D_{Eady} = \overline{\langle b_0\, \partial_x p_0 \rangle} = \overline{\langle b_{-1}\, \partial_x p_{-1} \rangle}\,, \tag{2.4}$$

where the zonal derivative of pressure corresponds to the meridional QG flow, the angular brackets denote horizontal area average, and the overbar denotes time average in the statistically steady regime.

2.2. *The 2LQG model*

The 2LQG model corresponds to further simplification as compared to the Eady model. As with the Eady model, we only discuss the main characteristics of the 2LQG model, redirecting the interested reader to standard textbooks for explicit derivations (Salmon 1998; Pedlosky 2013; Vallis 2017). The model is sketched in figure 1(*b*). A shallow fluid layer of uniform density ρ_1 sits above a shallow fluid layer of density $\rho_2 > \rho_1$, both layers having equal depth at rest. The fluid layers are subject to gravity and uniform global rotation around the vertical axis at a rate $f/2$, where f denotes the Coriolis parameter. We focus on the limit of rapid rotation and shallow fluid layers, so that the system is governed by QG dynamics. The Rossby deformation radius of the 2LQG model is $\lambda = \sqrt{g'H}/(2f)$, with $g' = (\rho_2 - \rho_1)g/\rho_1$ the reduced gravity.

https://doi.org/10.1017/jfm.2026.11943 Published online by Cambridge University Press

We denote as $\boldsymbol{u}_1(x, y, t)$ and $\boldsymbol{u}_2(x, y, t)$ the lowest-order velocity fields in the upper and lower layers, respectively. The velocity fields $\boldsymbol{u}_1$ and $\boldsymbol{u}_2$ are horizontal, vertically invariant and divergence-free in the horizontal plane. They derive from streamfunctions $\psi_1(x, y, t)$ and $\psi_2(x, y, t)$, i.e. $\boldsymbol{u}_{1,2} = -\boldsymbol{\nabla} \times (\psi_{1,2}\, \boldsymbol{e}_z)$. The base state consists of a vertically sheared zonal flow with uniform velocities $+U\boldsymbol{e}_x$ and $-U\boldsymbol{e}_x$ in the upper and lower layers, respectively. As a consequence of geostrophic and hydrostatic balance, the vertical displacement of the interface from its rest position is directly proportional to $\psi_1 - \psi_2$. The vertically sheared base flow corresponds to $\psi_1 - \psi_2 = -2Uy$, therefore the interface between the two layers is tilted in the meridional direction (see figure 1). This tilt of the interface corresponds to a uniform meridional gradient of vertically averaged buoyancy, in thermal-wind balance with the vertically sheared zonal flow.

We consider arbitrary departures from the base state, expressed in terms of two fields $\psi(x, y, t)$ and $\tau(x, y, t)$ defined by $(\psi_1 + \psi_2)/2 = \psi$ and $(\psi_1 - \psi_2)/2 = -Uy + \tau$. The field $\psi(x, y, t)$ is referred to as the 'barotropic' streamfunction. It corresponds to the streamfunction of the vertically averaged flow (average over both layers). The field $\tau(x, y, t)$ is the departure 'baroclinic' streamfunction. It encodes the departure of the vertically averaged buoyancy from its base-state uniform gradient. Because of this correspondence between τ and the vertically averaged buoyancy, τ is sometimes referred to as the buoyancy variable, even though it has the dimensions of a streamfunction. Correspondingly, U will sometimes be referred to as the background meridional buoyancy gradient in the following.

The QG expansion turns the shallow-water equations into conservation equations for the potential vorticities in both layers. The sum and difference of these equations yield the coupled evolution equations for ψ and τ, known as the barotropic PV and baroclinic PV equations. Non-dimensionalising space with λ and time with λ/U, these equations read

$$\partial_t \Delta\psi + J(\psi, \Delta\psi) + J(\tau, \Delta\tau) + \partial_x \Delta\tau = \mathcal{D}, \tag{2.5}$$

$$\partial_t(\Delta\tau - \tau) + J(\psi, \Delta\tau - \tau) + J(\tau, \Delta\psi) + \partial_x(\Delta\psi + \psi) = -\mathcal{D}. \tag{2.6}$$

We have included in the model a quadratic drag force in the lower layer, proportional to the squared lower-layer departure velocity. This drag term leads to the contributions $\pm\mathcal{D}$ on the right-hand sides of (2.5) and (2.6), where

$$\mathcal{D} = -\frac{\mu_*}{2}\boldsymbol{\nabla} \cdot [|\boldsymbol{\nabla}(\psi - \tau)|\, \boldsymbol{\nabla}(\psi - \tau)], \tag{2.7}$$

with μ_* the quadratic drag coefficient non-dimensionalised with λ. (In the following, $(\cdot)_*$ denotes quantities made dimensionless using U and λ.)

We are interested in the long-time statistics of solutions to (2.5) and (2.6) in a doubly periodic domain $x, y \in [0, L]^2$, with large-enough dimensionless domain size $L = \mathcal{L}/\lambda$ for these statistics to be independent of L. The main quantity of interest is the meridional buoyancy flux induced by the turbulent flow in statistically steady state. Non-dimensionalising this flux with U and λ leads to the effective diffusivity $D_* = \langle \overline{\psi_x \tau} \rangle$. The single emergent quantity D_* characterises the release of available potential energy from the baroclinically unstable background, the ensuing energy dissipation by bottom drag, and the overall transport properties of the system (Thompson & Young 2006).

When simulating this system numerically, for numerical stability we also include hyperviscous terms $-\nu\, \Delta^4(\Delta\psi)$ and $-\nu\, \Delta^4(\Delta\tau - \tau)$ on the right-hand sides of (2.5) and (2.6), respectively. We focus on the regime where the hyperviscosity ν is small enough for D_* to be independent of ν. Investigating the efficiency of the turbulent transport then

https://doi.org/10.1017/jfm.2026.11943 Published online by Cambridge University Press

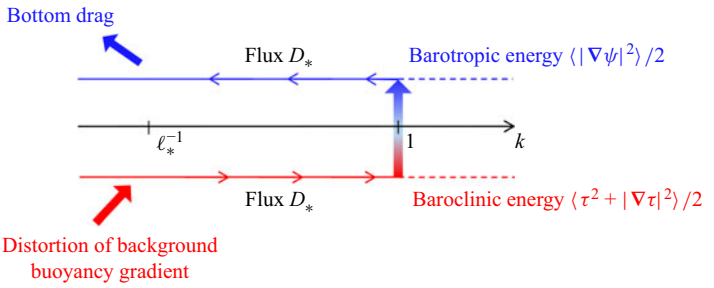


Figure 2. Energy cascades in baroclinic QG turbulence, as described in Salmon (1978). According to this scenario, energy conversion from the baroclinic mode to the barotropic mode arises near the Rossby deformation radius λ.

boils down to characterising the dependence of the dimensionless diffusivity D_* with the dimensionless drag coefficient μ_*.

2.3. *Turbulent cascades in the 2LQG model*

In a similar fashion to the 2-D Navier–Stokes (2DNS) equation, the inviscid, undamped 2LQG model features both an energy and an enstrophy invariant. The energy equation is obtained by multiplying (2.5) with ψ and (2.6) with τ, before summing the resulting equations and averaging over the domain:

$$\frac{\mathrm{d}}{\mathrm{d}t}\left[\frac{\langle|\nabla\psi|^2\rangle}{2}+\frac{\langle|\nabla\tau|^2\rangle}{2}+\frac{\langle\tau^2\rangle}{2}\right]=\langle\psi_x\tau\rangle+\langle(\tau-\psi)\mathcal{D}\rangle, \tag{2.8}$$

where we omit the negligible contribution from hyperviscosity. The three terms inside the square brackets respectively correspond to barotropic kinetic energy, baroclinic kinetic energy and potential energy. Time averaging in the statistically steady state leads to the energy power integral

$$D_*=\left\langle\overline{(\psi-\tau)\mathcal{D}}\right\rangle, \tag{2.9}$$

relating the rate of release of potential energy $D_*=\langle\overline{\psi_x\tau}\rangle$ to the power dissipated by the drag term. The precise energy pathways in 2LQG turbulence are represented schematically in figure 2, adapted from the work of Salmon (1978, 1980). When the drag coefficient is small, the flow develops large structures up to a typical scale $\ell\gg\lambda$, denoted as $\ell_*=\ell/\lambda\gg1$ in dimensionless form. The large-scale flow distorts the background gradient of τ through the term $\partial_x\psi$ in (2.6). This process is a source of baroclinic potential energy (also known as eddy available potential energy; see Lobo 2025), associated with the injection term $D_*=\langle\overline{\psi_x\tau}\rangle$ on the left-hand side of the energy power integral (2.9). The input potential energy $\langle\tau^2\rangle/2$ follows a forward cascade from the large scale ℓ (dimensionless scale ℓ_*) down to smaller scales. However, as for standard 2DNS turbulence, the conservation of both energy and enstrophy forbids the forward energy cascade reaching all the way to the small hyperviscous scale. Instead, the forward cascade of baroclinic potential energy stops at scales comparable to the deformation radius (dimensionless scale 1), where baroclinic energy is efficiently converted into barotropic kinetic energy. The latter then obeys an inverse cascade akin to the standard inverse energy cascade of the 2DNS equation. Barotropic energy is transferred all the way up to the large scale ℓ_* where drag efficiently dissipates it. In turn, the large-scale barotropic flow distorts the background gradient of τ, feeding once again the forward cascade of potential energy.

https://doi.org/10.1017/jfm.2026.11943 Published online by Cambridge University Press

The frictional sink in the power integral (2.9) is thus dominated by the contribution from the barotropic flow,

$$\left\langle \overline{(\psi-\tau)\mathcal{D}} \right\rangle = -\frac{\mu_*}{2}\left\langle \overline{(\psi-\tau)\boldsymbol{\nabla}\cdot[|\boldsymbol{\nabla}(\psi-\tau)|\,\boldsymbol{\nabla}(\psi-\tau)]} \right\rangle$$
$$\simeq -\frac{\mu_*}{2}\left\langle \overline{\psi\boldsymbol{\nabla}\cdot[|\boldsymbol{\nabla}\psi|\,\boldsymbol{\nabla}\psi]} \right\rangle = \frac{\mu_*}{2}\left\langle \overline{|\boldsymbol{\nabla}\psi|^3} \right\rangle. \tag{2.10}$$

The power integral thus reflects a balance between the rate of release of potential energy due the distortion of the background buoyancy gradient by the large-scale barotropic flow, and the rate of damping of barotropic kinetic energy through bottom friction.

2.4. *Vortex-gas scaling theory*

The turbulent cascade phenomenology of Salmon provides invaluable insight into the qualitative behaviour of the 2LQG system. However, it proves insufficient to make quantitative predictions for the turbulent transport properties of the system (Chang & Held 2019, 2021; Chen 2023), namely for the scaling relation between D_* and μ_*. The reason is that the cascade theory is framed in spectral space, therefore it misses any large-scale organisation of the flow in physical space. As observed by Thompson & Young (2006), however, the large-scale barotropic flow organises into a dilute vortex gas, i.e. an ensemble of vortices with a core radius much smaller than the typical distance $\ell_* \gg 1$ between two vortices. The coherent vortices are crucial because even though the vortex cores occupy a small fraction of the area of the domain, they are responsible for most of the frictional dissipation (2.10) entering the power integral (2.9) (Hadjerci & Gallet 2023). Such large-scale flow organisation into a vortex gas is by no means a property of the 2LQG model only. Indeed, we recently showed that the same phenomenology arises in the standard 2DNS equation, with important consequences for the transport properties of the flow (Meunier & Gallet 2025).

3. Reduced equations for 2LQG baroclinic turbulence at low drag

Before mapping the Eady model onto the 2LQG model, a preliminary step is to reduce the latter model by retaining only the dominant terms controlling the low-drag dynamics. To identify the dominant terms of (2.5)–(2.6) at the 'large scale' ℓ_* and at the 'small scale' 1 (corresponding to the deformation radius in dimensional form), we first provide estimates for the various fields and their derivatives. The estimates at scale ℓ_* are denoted with a subscript LS for 'large-scale estimate', while the estimates at scale 1 are denoted with a subscript SS for 'small-scale estimate'.

3.1. *Estimating large-scale quantities in the 2LQG model: the vortex-gas model*

In the present 2LQG context, the vortex-gas scaling theory was initially put forward in Gallet & Ferrari (2020), before being refined in Hadjerci & Gallet (2023) to capture the regime of very-low quadratic drag. For the sake of brevity, we only recall here the main scaling relations without justification, referring the interested reader to Gallet & Ferrari (2020), Hadjerci & Gallet (2023) and Meunier & Gallet (2025) for the detailed scaling arguments. The barotropic flow consists of a gas of vortices, with typical inter-vortex distance $\ell_* \gg 1$ and core radius scaling as $\sqrt{\ell_*}$. In the spectral-space picture depicted in figure 2, the latter scale is intermediate between the large inter-vortex distance ℓ_* and the small Rossby deformation radius (dimensionless scale 1). The barotropic streamfunction has typical magnitude $\psi_{LS} \sim \ell_*^2$. Correspondingly, the typical velocity in the inter-vortex region is $(\boldsymbol{\nabla}\psi)_{LS} \sim \ell_*$. The effective diffusivity D_* of the flow scales as the product

https://doi.org/10.1017/jfm.2026.11943 Published online by Cambridge University Press

	$\boldsymbol{\nabla}$	∂_t	ψ	$\boldsymbol{\nabla}\psi$	$\Delta\psi$	τ	$\boldsymbol{\nabla}\tau$	$\Delta\tau$
LS estimates	ℓ_*^{-1}	1	ℓ_*^2	ℓ_*	1	ℓ_*	1	ℓ_*^{-1}
SS estimates	1	ℓ_*	$\ell_*^{2/3}$	$\ell_*^{2/3}$	$\ell_*^{2/3}$	$\ell_*^{2/3}$	$\ell_*^{2/3}$	$\ell_*^{2/3}$

Table 1. Estimates of the various fields and their space and time derivatives in the inter-vortex region, both at the large dimensionless scale ℓ_* (LS) and at the small dimensionless scale 1 associated with the deformation radius (SS). The scalings are reported in terms of powers of the large scale $\ell_* \gg 1$. Scaling laws in terms of the dimensionless quadratic drag coefficient are obtained by substituting the vortex-gas scaling prediction $\ell_* \sim \mu_*^{-2/3}$.

of this large-scale velocity with the large scale ℓ_* of the flow, which leads to $D_* \sim \ell_*^2$. The baroclinic streamfunction scales as $\tau_{LS} \sim \ell_*$, as deduced from a slantwise free-fall argument in e.g. Gallet & Ferrari (2020). Such fluctuations of τ are produced at the large scale ℓ_* through the distortion of the background gradient by the vortex-gas flow. These estimates are gathered in the first row of table 1. We also include the scaling $\boldsymbol{\nabla}_{LS} \sim \ell_*^{-1}$ for the spatial derivatives at large scale, and a scaling of the time derivative based on the typical turnover time of the large-scale barotropic flow, $(\partial_t)_{LS} \sim (\boldsymbol{\nabla}\psi)_{LS}/\ell_* \sim 1$.

3.2. *Estimating small-scale quantities in the 2LQG model: Salmon's dual cascade theory*

We now consider spatial scales comparable to the deformation radius, referred to as 'small scales' in the following, the deformation radius being much smaller than the integral scale of the flow (i.e. $\ell_* \gg 1$ in dimensionless form). With our non-dimensionalisation, such scales correspond to spatial derivatives of order $\boldsymbol{\nabla}_{SS} \sim 1$. Estimates for ψ and τ at the deformation scale can be readily obtained from Salmon's dual cascade theory. For the inverse energy cascade of barotropic kinetic energy, a standard 'Kolmogorov' estimate for the velocity increment at scale r is $\delta(|\boldsymbol{\nabla}\psi|) \sim (D_* r)^{1/3}$, where δ denotes the two-point increment over a dimensionless separation r, and D_* denotes the dimensionless energy flux (usually denoted as ϵ in the standard literature). Upon substituting $r = \ell_*$ and $r = 1$, and taking the ratio of the resulting expressions, we obtain

$$\frac{(\boldsymbol{\nabla}\psi)_{LS}}{(\boldsymbol{\nabla}\psi)_{SS}} \sim \ell_*^{1/3} \quad \Rightarrow \quad (\boldsymbol{\nabla}\psi)_{SS} \sim \ell_*^{2/3}, \tag{3.1}$$

where we used $(\boldsymbol{\nabla}\psi)_{LS} \sim \ell_*$. Combining (3.1) with $\boldsymbol{\nabla}_{SS} \sim 1$ yields $\psi_{SS} \sim \ell_*^{2/3}$. In a similar fashion, the forward cascade of temperature variance τ^2 leads to the following estimate for the temperature increment $|\delta\tau| \sim (D_* r)^{1/3}$, where D_* denotes the dimensionless flux of temperature variance (see figure 2). Substituting $r = \ell_*$ and $r = 1$ and dividing the resulting expressions leads to

$$\frac{\tau_{LS}}{\tau_{SS}} \sim \ell_*^{1/3} \quad \Rightarrow \quad \tau_{SS} \sim \ell_*^{2/3}, \tag{3.2}$$

where we have inserted $\tau_{LS} \sim \ell_*$ to obtain the second expression. Finally, we estimate the time derivative of small-scale quantities based on their advection by the fast large-scale barotropic flow (advection by the small-scale barotropic flow being subdominant): $(\partial_t)_{SS} \sim (\boldsymbol{\nabla}\psi)_{LS} \cdot \boldsymbol{\nabla}_{SS} \sim \ell_*$. The estimates for ψ, τ and their derivatives at small scale are reported in the second row of table 1.

https://doi.org/10.1017/jfm.2026.11943 Published online by Cambridge University Press

3.3. *Reduced equations*

Starting from the undamped 2LQG equations, the first step of the reduction consists in identifying the dominant terms at the beginning and end of the turbulent cascades (scales ℓ_* and 1). By forming reduced equations that retain such dominant terms at both ends of the cascades, we should capture the right dynamics throughout the inertial ranges of the cascades.

Let us proceed by considering first the undamped version of the τ equation:

$$\partial_t(\Delta\tau - \tau) + J(\psi, \Delta\tau - \tau) + J(\tau, \Delta\psi) + \partial_x(\Delta\psi + \psi) = 0. \tag{3.3}$$

At the large scale ℓ_*, following table 1, the various terms scale as follows:

$$\partial_t(\Delta\tau) \sim \ell_*^{-1}, \quad \partial_t\tau \sim \ell_*, \tag{3.4}$$

$$J(\psi, \Delta\tau) \sim \ell_*^{-1}, \quad J(\psi, \tau) \sim \ell_*, \tag{3.5}$$

$$J(\tau, \Delta\psi) \sim \ell_*^{-1}, \quad \partial_x\Delta\psi \sim \ell_*^{-1}, \quad \partial_x\psi \sim \ell_*, \tag{3.6}$$

meaning that only the terms $-\partial_t\tau$, $-J(\psi, \tau)$ and $\partial_x\psi$ need be retained to describe the large-scale dynamics of τ. This aligns well with the standard phenomenology (Salmon 1978, 1980; Larichev & Held 1995). Namely, the temperature field behaves as a passive scalar at large scales, with fluctuations induced by the distortion of the background temperature gradient by the barotropic flow (Thompson & Young 2006; Gallet & Ferrari 2020).

At the small dimensionless scale 1 (deformation radius), following table 1, the various terms are estimated as follows:

$$\partial_t(\Delta\tau - \tau) \sim \ell_*^{5/3}, \quad J(\psi, \Delta\tau - \tau) \sim (\boldsymbol{\nabla}\psi)_{LS}\boldsymbol{\nabla}(\Delta\tau - \tau)_{SS} \sim \ell_*^{5/3}, \tag{3.7}$$

$$J(\tau, \Delta\psi) \sim \ell_*^{4/3}, \quad \partial_x(\Delta\psi + \psi) \sim \ell_*^{2/3}, \tag{3.8}$$

meaning that only the terms $\partial_t(\Delta\tau - \tau)$ and $J(\psi, \Delta\tau - \tau)$ need be retained to describe the small-scale dynamics of τ. Including in a single equation the dominant terms at large scale and the dominant terms at small scale leads to the following reduced undamped equation:

$$\partial_t(\Delta\tau - \tau) + J(\psi, \Delta\tau - \tau) + \partial_x\psi = 0. \tag{3.9}$$

We now turn to the undamped version of the ψ equation:

$$\partial_t\Delta\psi + J(\psi, \Delta\psi) + J(\tau, \Delta\tau) + \partial_x\Delta\tau = 0. \tag{3.10}$$

At the large scale ℓ_*, following table 1, the various terms scale as follows:

$$\partial_t\Delta\psi \sim 1, \quad J(\psi, \Delta\psi) \sim 1, \tag{3.11}$$

$$J(\tau, \Delta\tau) \sim \ell_*^{-2}, \quad \partial_x\Delta\tau \sim \ell_*^{-2}, \tag{3.12}$$

meaning that only the terms $\partial_t\Delta\psi$ and $J(\psi, \Delta\psi)$ need be retained to describe the large-scale dynamics of ψ. At the small dimensionless scale 1 (deformation radius), following table 1, the various terms are estimated as follows:

$$\partial_t\Delta\psi \sim \ell_*^{5/3}, \quad J(\psi, \Delta\psi) \sim (\boldsymbol{\nabla}\psi)_{LS}\boldsymbol{\nabla}\Delta\psi_{SS} \sim \ell_*^{5/3}, \tag{3.13}$$

$$J(\tau, \Delta\tau) \sim (\boldsymbol{\nabla}\tau)_{SS}\boldsymbol{\nabla}\Delta\tau_{SS} \sim \ell_*^{4/3}, \quad \partial_x\Delta\tau \sim \ell_*^{2/3}. \tag{3.14}$$

https://doi.org/10.1017/jfm.2026.11943 Published online by Cambridge University Press

The dominant terms lead to the 2-D Euler equation for ψ:

$$\partial_t \Delta\psi + J(\psi, \Delta\psi) = 0. \tag{3.15}$$

By keeping the lowest-order terms of each equation, we have reduced the system to an unforced, undamped Euler flow (3.15) that distorts the background gradient of some passive scalar field $\Delta\tau - \tau$; see (3.9). The above Euler equation for ψ, uncoupled to τ, cannot capture the dynamics of the full 2LQG system. Instead, in line with the analytical treatment of weakly forced and damped systems, such a lowest-order Euler equation must typically be complemented by a solvability condition arising at next order; the weak forcing and dissipative terms then come into play to enforce the energy power integral, thus selecting the correct flow solution (Fauve & Thual 1990; Sprague *et al.* 2006; Julien & Knobloch 2007; Gallet & Young 2013; Gallet 2024). In the present context, according to Salmon's phenomenology, the barotropic flow is forced at small scale through conversion of energy from the baroclinic component τ, and it is damped at large scale by friction. We thus complement (3.15) with the first next-order term at small scale, $J(\tau, \Delta\tau)$ (see the estimates (3.14)), together with the lowest-order expression of the large-scale friction term, $\mathcal{D} \simeq -(\mu_*/2)\,\boldsymbol{\nabla}\cdot(|\boldsymbol{\nabla}\psi|\,\boldsymbol{\nabla}\psi)$. In contrast with (3.15), (3.9) already includes the dominant sources and sinks of baroclinic energy, therefore it does not require the inclusion of higher-order terms. The result of this procedure is the following reduced set of equations:

$$\partial_t \Delta\psi + J(\psi, \Delta\psi) + J(\tau, \Delta\tau) = -\frac{\mu_*}{2}\boldsymbol{\nabla}\cdot(|\boldsymbol{\nabla}\psi|\,\boldsymbol{\nabla}\psi) - \nu\,\Delta^5\psi, \tag{3.16}$$

$$\partial_t(\Delta\tau - \tau) + J(\psi, \Delta\tau - \tau) + \partial_x\psi = -\nu\,\Delta^4(\Delta\tau - \tau), \tag{3.17}$$

where we have also included the hyperviscous terms to damp vorticity filaments and ensure numerical stability.

A few remarks are in order. First, as for the initial set of equations, the reduced equations above conserve mechanical energy in the undamped, inviscid limit. The corresponding energy equation is (2.8), in which we substitute the (instantaneous version of) approximation (2.10). Second, as a sanity check, we can estimate the rate of baroclinic-to-barotropic energy conversion $\langle\psi\, J(\tau, \Delta\tau)\rangle$ induced by the term $J(\tau, \Delta\tau)$. Based on table 1, we obtain $\langle\psi\, J(\tau, \Delta\tau)\rangle \sim \ell_*^2$. This energy conversion rate is also proportional to the overall meridional heat flux in the system. It is therefore equal to the dimensionless diffusivity D_*. We thus recover the scaling relation $D_* \sim \ell_*^2$ obtained in the context of the vortex-gas scaling theory (Gallet & Ferrari 2020), while a close relation involving the energy-containing scale was discussed by Larichev & Held (1995) before that. Third, and more surprisingly, the equations above lack some of the linear terms that are crucial for baroclinic instability (compare with (2.5), (2.6)). That is, the linearised versions of (3.16)–(3.17) feature no exponentially growing modes. If initialised with energetic enough initial conditions, however, a numerical simulation of (3.16)–(3.17) sustains a turbulent state indefinitely, in a 'subcritical' fashion, and this turbulent state closely resembles that of the full 2LQG system. To illustrate this point, we have run a suite of such numerical simulations with weak hyperviscosity, varying the drag coefficient (see § 5.2 for details on the numerical procedure). As shown in figure 5 below, for low drag, the resulting diffusivity D_* agrees quantitatively with the values obtained from simulations of the full 2LQG model (2.5)–(2.6). We thus conclude that linear instability plays no role in the energy looping pathways described by Salmon, nor in setting the overall transport properties of the 2LQG system; instead, the turbulent state self-sustains in a subcritical way. On the one hand, this could explain why baroclinic turbulence appears qualitatively different from simulations of the 2DNS equation forced by a small-scale instability mechanism (van Kan *et al.* 2022). On the other hand, driving the 2DNS equation with

https://doi.org/10.1017/jfm.2026.11943 Published online by Cambridge University Press

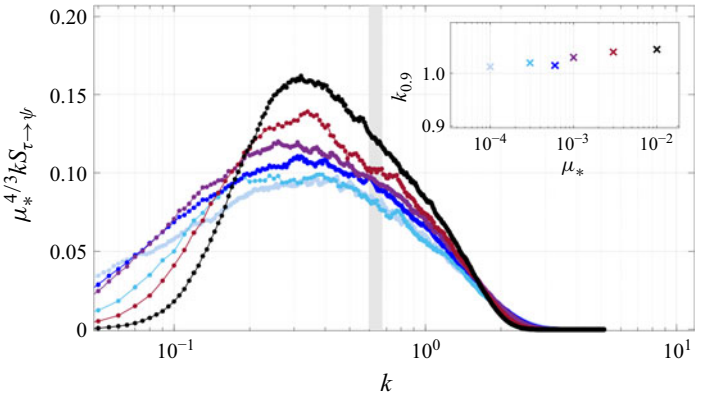


Figure 3. Pre-multiplied cross-spectra $S_{\tau\to\psi}(k)$ from the 2LQG model, rescaled using the power law $D_* \sim \mu_*^{-4/3}$ of the overall energy conversion rate. Colour encodes the dimensionless drag μ_*, with values shown in the inset. The grey-shaded interval corresponds to the range spanned by the injection wavenumber k_Ω obtained from the ratio of barotropic enstrophy injection rate to barotropic energy injection rate (see text). The inset shows the wavenumber $k_{0.9}$ as a function of dimensionless drag, defined such that 90 % of energy injection into the barotropic flow arises from wavenumbers $k \leqslant k_{0.9}$.

a small-scale body force (be it steady or δ-correlated in time) leads to a flow that is fully compatible with the vortex-gas description of baroclinic turbulence, both qualitatively and quantitatively (Meunier & Gallet 2025). Why linear instability and body force lead to such different end states, and why the latter better represents the subcritical sustainment of turbulence in (3.16)–(3.17), remain to be further investigated.

4. Large-scale expansion of the Eady model

The next step of the mapping procedure consists of a large-scale expansion of the Eady model. To motivate this expansion, we first discuss the scale of energy conversion in our suite of numerical simulations of the 2LQG model. For brevity, we defer the discussion on numerical methods to § 5.2, where the simulations of all three models are described together.

4.1. *Preamble: the scales of energy conversion*

The scale dependence of the baroclinic-to-barotropic energy conversion in the 2LQG model is investigated using the cross-spectrum $S_{\tau\to\psi}(k)$ between ψ and $J(\tau, \Delta\tau)$, defined such that $\int_0^\infty S_{\tau\to\psi}(k)\,\mathrm{d}k = \langle \psi\, J(\tau, \Delta\tau)\rangle$ (in line with the reduction in § 3, we neglect $\partial_x \Delta\tau$ as compared to the dominant term $J(\tau, \Delta\tau)$). Figure 3 shows the pre-multiplied cross-spectra $k\, S_{\tau\to\psi}(k)$ computed for friction coefficients ranging from $\mu_* = 10^{-4}$ to $\mu_* = 10^{-2}$. A key observation is that the energy transfers correspond mostly to wavenumbers $k \leqslant 1$, as illustrated by the fact that the pre-multiplied spectra have weight mostly for wavenumbers $k \leqslant 1$.

To make this point more quantitative, we define $k_{0.9}$ as the wavenumber such that $\int_0^{k_{0.9}} S_{\tau\to\psi}(k)\,\mathrm{d}k = 0.9\langle \psi\, J(\tau, \Delta\tau)\rangle$. That is, 90 % of energy injection into the barotropic flow is due to wavenumbers $k \leqslant k_{0.9}$. As shown in the inset of figure 3 for the 2LQG simulations, $k_{0.9}$ is close to 1, with an approximately constant value in the low-drag limit. Also shown in figure 3 is a characteristic injection wavenumber k_Ω for the barotropic flow of the reduced model, based on the ratio of the injection rate of barotropic enstrophy to the

https://doi.org/10.1017/jfm.2026.11943 Published online by Cambridge University Press

injection rate of barotropic energy (dominant terms only):

$$k_\Omega = \sqrt{-\left\langle \overline{J(\tau,\,\Delta\tau)\,\Delta\psi} \right\rangle / \left\langle \overline{J(\tau,\,\Delta\tau)\,\psi} \right\rangle}. \tag{4.1}$$

As shown in figure 3, the latter is approximately constant in the low-drag regime, with $k_\Omega \simeq 0.6$.

Our strategy for establishing a mapping between the Eady and 2LQG models is as follows. Based on the observation that energy injection into the barotropic mode is due to wavenumbers $k \lesssim 1$ in both the 2LQG model (2.5)–(2.6) and the reduced model (3.16)–(3.17), we perform a low-k expansion of the inversion relation (2.3) of the Eady model: $k/\tanh k \simeq 1 + k^2/3$ and $k/\sinh k \simeq 1 - k^2/6$, with 96 % accuracy for $k \leqslant 1.2$. In § 4.2, we show that such a low-k expansion turns the Eady model into a set of equations that closely resembles the 2LQG system. The connection is made explicit by changing variables to show that the large-scale expansion of the Eady model leads to the same reduced set (3.16)–(3.17) as the 2LQG model, with explicit expressions for the control parameters of the Eady model in terms of those of the 2LQG model. The reduced equations for the Eady model thus correspond to energy injection into the barotropic mode at scales $k \lesssim 1$, which justifies the low-k expansion *a posteriori*, in a self-consistent fashion. Reducing the two models to the same set of equations allows us to quantitatively predict the transport properties of the Eady model from the knowledge of the scaling laws of the 2LQG model only. We validate these predictions numerically in § 5.2 using simulations of both the 2LQG and Eady models.

4.2. *Reduction of the Eady model*

Expanding the inversion matrix in (2.3) to order k^2 yields

$$\begin{pmatrix} \hat{b}_0|_{\boldsymbol{k}} \\ \hat{b}_{-1}|_{\boldsymbol{k}} \end{pmatrix} = \begin{bmatrix} 1 + \dfrac{k^2}{3} & -1 + \dfrac{k^2}{6} \\ 1 - \dfrac{k^2}{6} & -1 - \dfrac{k^2}{3} \end{bmatrix} \begin{pmatrix} \hat{p}_0|_{\boldsymbol{k}} \\ \hat{p}_{-1}|_{\boldsymbol{k}} \end{pmatrix}, \tag{4.2}$$

which we recast in physical space using the Laplacian operator Δ:

$$\begin{pmatrix} b_0 \\ b_{-1} \end{pmatrix} = \begin{bmatrix} 1 - \dfrac{\Delta}{3} & -1 - \dfrac{\Delta}{6} \\ 1 + \dfrac{\Delta}{6} & -1 + \dfrac{\Delta}{3} \end{bmatrix} \begin{pmatrix} p_0 \\ p_{-1} \end{pmatrix}. \tag{4.3}$$

The inversion relation above somewhat resembles that of the 2LQG system, where b_0 plays a role similar to q_1, and $-b_{-1}$ plays a role similar to q_2. To make this similarity visible, we change variables to

$$\tilde{\boldsymbol{x}} = \sqrt{12}\,\boldsymbol{x}, \quad \tilde{\psi} = 6(p_0 + p_{-1}), \quad \tilde{\tau} = \sqrt{12}\,(p_0 - p_{-1}), \quad \tilde{t} = t, \quad \tilde{\mu} = \frac{\mu_{Eady}}{\sqrt{3}}, \tag{4.4}$$

where $\boldsymbol{x} = (x,\, y)$ denotes the horizontal coordinates.

Substitution into (2.1)–(2.2) and in the expanded inversion relation (4.3) allows us to recast the governing equations in terms of the new variables. Dropping the tildes for brevity, after lengthy but straightforward calculations we obtain

https://doi.org/10.1017/jfm.2026.11943 Published online by Cambridge University Press

$$\partial_t \Delta\psi + J(\psi, \Delta\psi) + J(\tau, \Delta\tau) + \partial_x \Delta\tau = -\frac{\mu}{2}\boldsymbol{\nabla}\cdot\Big[|\boldsymbol{\nabla}(\psi - \sqrt{3}\,\tau)|\,\boldsymbol{\nabla}(\psi - \sqrt{3}\,\tau)\Big], \tag{4.5}$$

$$\partial_t(\tau - \Delta\tau) + J(\psi, \tau - \Delta\tau) - \partial_x\psi - 3\,\partial_x\Delta\psi - 3\,J(\tau, \Delta\psi) = -\frac{\sqrt{3}\,\mu}{2}\boldsymbol{\nabla}\cdot\Big[|\boldsymbol{\nabla}(\psi - \sqrt{3}\,\tau)|\,\boldsymbol{\nabla}(\psi - \sqrt{3}\,\tau)\Big]. \tag{4.6}$$

The last step consists in performing the same reduction of (4.5)–(4.6) as for the 2LQG model. Namely, following the same steps as in § 3, we neglect the term $\partial_x\Delta\tau$ in (4.5) and the terms $-3\,\partial_x\Delta\psi - 3\,J(\tau, \Delta\psi)$ in (4.6). Additionally, we neglect the drag term in (4.6) while retaining only the (dominant) contribution from ψ in the drag term of (4.5). Following these simplifications, (4.5)–(4.6) reduce to the exact same equations (3.16)–(3.17) as for the 2LQG model, with μ playing the role of μ_*.

5. Eady diffusivity inferred from the equivalent 2LQG system

5.1. *Theoretical prediction*

The mapping readily provides a way of determining the effective diffusivity of the Eady model in terms of that of the 2LQG model. We thus assume that we know the functional dependence of the 2LQG effective diffusivity $D_*(\mu_*)$ with the dimensionless friction coefficient μ_*. Our goal is to deduce the Eady effective diffusivity $D_{Eady}(\mu_{Eady})$ in terms of the dimensionless friction coefficient μ_{Eady} of the Eady model. We start from (2.4) under the form $D_{Eady} = \overline{\langle b_0\,\partial_x p_0\rangle}$. Substituting (4.3) for b_0 in terms of p_0 and p_{-1} leads to

$$D_{Eady} = -\left\langle\overline{\partial_x(p_0)\,p_{-1}}\right\rangle - \left\langle\overline{\partial_x(p_0)\,\Delta(p_{-1})}\right\rangle/6. \tag{5.1}$$

The change of variables (4.4) corresponds to $p_0 = \tilde{\psi}/12 + \tilde{\tau}/(4\sqrt{3})$, $p_{-1} = \tilde{\psi}/12 - \tilde{\tau}/(4\sqrt{3})$, and spatial derivatives rescale according to $\partial_{x_i} = 2\sqrt{3}\,\partial_{\tilde{x}_i}$. Substituting into (5.1) and dropping the tildes yields

$$D_{Eady} = \frac{\overline{\langle\psi_x\,\tau\rangle}}{12} + \frac{\overline{\langle\psi_x\,\Delta\tau\rangle}}{6}. \tag{5.2}$$

According to table 1, the term $\psi_x\tau$ scales as ℓ_*^2 at large scale, and as $\ell_*^{4/3}$ at small scale, while the term $\psi_x\,\Delta\tau$ scales as 1 at large scale, and as $\ell_*^{4/3}$ at small scale. We conclude that $\overline{\langle\psi_x\,\Delta\tau\rangle} \sim \ell_*^{4/3}$ is negligible as compared to $\overline{\langle\psi_x\,\tau\rangle} \sim \ell_*^2$ on the right-hand side of (5.2). To dominant order in $\ell_* \gg 1$, we finally obtain

$$D_{Eady}(\mu_{Eady}) = \frac{1}{12}D_*\big(\mu_* = \mu_{Eady}/\sqrt{3}\big), \tag{5.3}$$

where the expression for μ_* in terms of μ_{Eady} arises from (4.4). Equation (5.3) provides a parameter-free expression of the effective diffusivity of the Eady model, based on that of the 2LQG model. A low-drag asymptotic expression for the latter is provided by the vortex-gas scaling theory (Hadjerci & Gallet 2023):

$$D_*(\mu_*) = \frac{c_{2LQG}}{\mu_*^{4/3}}, \tag{5.4}$$

where the prefactor is $c_{2LQG} \simeq 0.3436$. Substitution into (5.3) yields the following asymptotic prediction for the effective diffusivity of the low-drag Eady model:

$$D_{Eady}(\mu_{Eady}) = \frac{c_{Eady}}{\mu_{Eady}^{4/3}}, \tag{5.5}$$

https://doi.org/10.1017/jfm.2026.11943 Published online by Cambridge University Press

with the prefactor $c_{Eady} = c_{2LQG}/(4 \times 3^{1/3}) \simeq 0.060$.

5.2. *Numerical validation*

With the goal of validating the predictions above, we performed suites of numerical simulations of the Eady model, of the 2LQG model, and of the reduced equations (3.16)–(3.17), varying the drag coefficient for all three models. The simulations employ standard pseudo-spectral methods with dealiasing and Runge–Kutta time-stepping. The doubly periodic domain is large enough for the effective diffusivity to be independent of domain size, and we employ low-enough hyperviscosity for the effective diffusivity to also be independent of hyperviscosity. The effective diffusivity is thus a function of the drag coefficient only. Snapshots of the instantaneous fields are provided in figure 4 for all three models in the low-drag regime. The fields look qualitatively similar, with a barotropic flow organised into a gas of coherent vortices. At the quantitative level, the raw dataset for diffusivity versus drag is shown in figure 5. In the low-drag regime, the curves $D_*(\mu_*)$ are extremely similar for the 2LQG model and for the reduced equations, which confirms that the latter correctly describe the low-drag dynamics of the full 2LQG model. By contrast, the curve $D_{Eady}(\mu_{Eady})$ departs from that of the other two models. Also shown are numerical simulations of an Eady model where the inversion relation (2.3) has been replaced by the large-scale expansion (4.3). The resulting eddy diffusivity closely agrees with D_{Eady}, which validates the large-scale expansion of the Eady model.

To test the predictions of the mapping procedure, in figure 5 we plot D_{Eady} against μ_{Eady}, together with the data of the 2LQG and reduced models plotted under the form $D_*/12$ against $\sqrt{3}\,\mu_*$. According to (5.3), we expect the data from all three models to collapse onto a master curve in the low-drag regime. Such a collapse of the whole dataset is indeed observed in figure 5, which validates the mapping procedure. Also shown in figure 5 is the low-drag asymptotic prediction (5.5) derived from the vortex-gas scaling theory. This prediction accurately captures the low-drag data, demonstrating how the 2LQG model can be used to make quantitative, parameter-free predictions for the Eady model.

6. Linear drag

While we have introduced the mapping procedure for an Eady model with quadratic drag, the approach readily carries over to linear bottom drag. The right-hand side of (2.2) is then replaced by $-\kappa_{Eady}\,\Delta p_{-1}$, where κ_{Eady} denotes the dimensionless linear drag coefficient (see Gallet *et al.* (2022) for a detailed description of the Eady model with linear bottom drag). For a 2LQG model with linear drag, the drag term entering (2.5)–(2.6) becomes $\mathcal{D} = -\kappa_*\,\Delta(\psi - \tau)$, where κ_* denotes the linear drag coefficient non-dimensionalised using U and λ. Following the steps in § 5, one obtains the reduced set (3.16)–(3.17), where the drag term is replaced by $-\kappa_*\,\Delta\psi$. Introducing the rescaled variables (4.4) with the additional relation $\tilde{\kappa} = \kappa_{Eady}$, one easily shows that the Eady model reduces to the same reduced equations as the 2LQG model. This mapping provides the following relation between the effective diffusivities of the Eady and 2LQG models with weak linear drag:

$$D_{Eady}(\kappa_{Eady}) = \frac{1}{12} D_* \left(\kappa_* = \kappa_{Eady}\right). \tag{6.1}$$

The vortex-gas theory applied to the 2LQG model leads to the scaling prediction $D_*(\kappa_*) = c_1 \exp(c_2/\kappa_*)$ for the effective diffusivity, where the numerical constants $c_1 = 1.7128$ and $c_2 = 0.7644$ have been adjusted to the numerical data in Hadjerci & Gallet (2023). Combining the knowledge of the 2LQG diffusivity with the mapping relation (6.1) leads to a quantitative prediction for the effective diffusivity of the Eady

https://doi.org/10.1017/jfm.2026.11943 Published online by Cambridge University Press

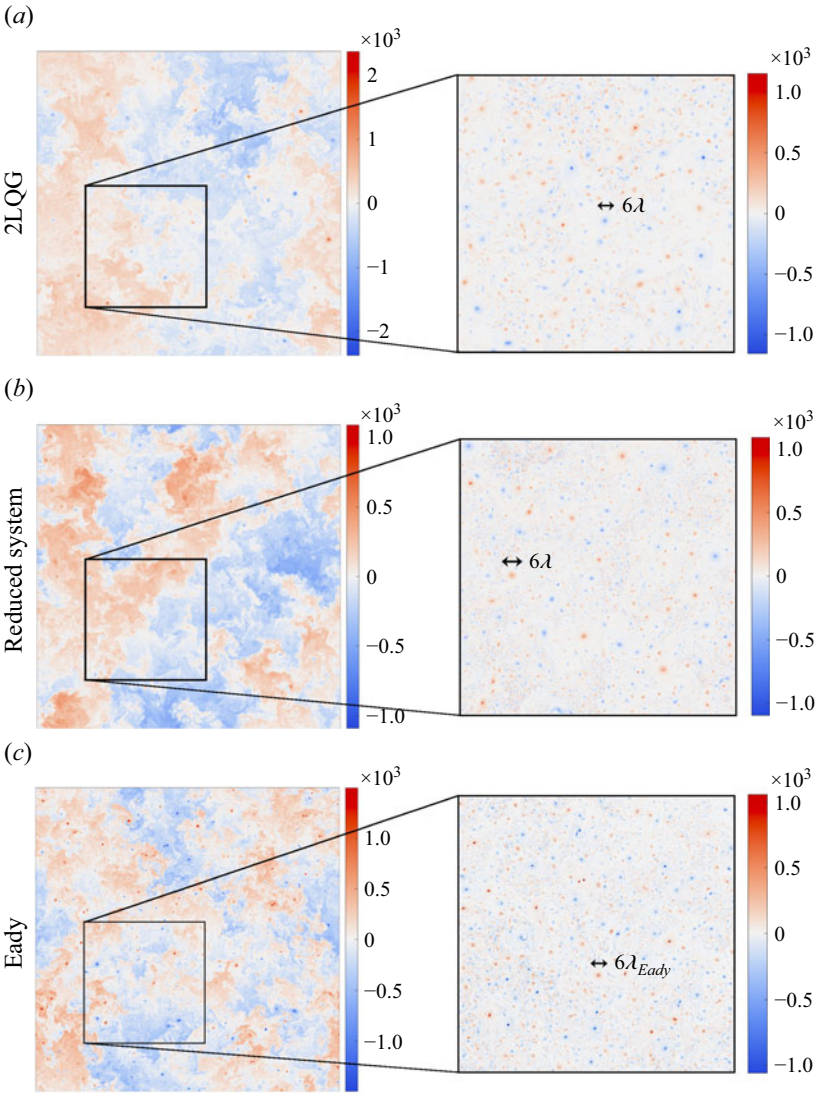


Figure 4. Snapshots from all three models. The left-hand panels of (*a*) and (*b*) show the baroclinic streamfunction τ from the 2LQG and reduced models, to be compared with their Eady counterpart $\tilde{\tau} = \sqrt{12}\,(p_0 - p_{-1})$, shown in the left-hand panel of (*c*). The right-hand panels of (*a*) and (*b*) show the barotropic vorticity $\Delta\psi$ from the 2LQG and reduced models in units of U/λ, to be compared with their Eady counterpart $b_{-1} - b_0$, shown in the right-hand panel of (*c*) in units of HSN. The drag is $\mu_* = 3 \times 10^{-4}$ in (*a*) and (*b*), and $\mu_{Eady} = 6 \times 10^{-4}$ in (*c*). The Eady simulation maps onto an effective friction $\mu_{Eady}/\sqrt{3} \simeq 3.5 \times 10^{-4}$ for the equivalent 2LQG system, in an effective simulation domain that is larger than that of simulations (*a*) and (*b*). Hence the smaller apparent flow scales in (*c*).

model with weak linear drag:

$$D_{Eady}(\kappa_{Eady}) = \frac{c_1}{12}\,\mathrm{e}^{c_2/\kappa_{Eady}} \simeq 0.1427\,\mathrm{e}^{0.7644/\kappa_{Eady}}. \tag{6.2}$$

In figure 6, we compare this prediction with numerical simulations of the QG Eady model with linear bottom drag. The numerical data correspond to the QG Eady simulations reported in Gallet *et al.* (2022), where we ran again the lowest-drag simulation using a

https://doi.org/10.1017/jfm.2026.11943 Published online by Cambridge University Press

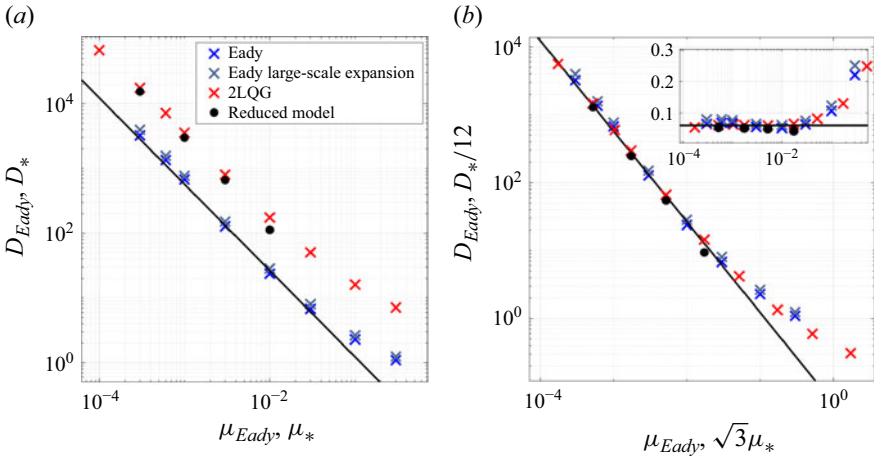


Figure 5. Effective diffusivity versus quadratic drag coefficient from numerical simulations of the Eady model (dark blue), of the expanded Eady model using inversion relation (4.2) (grey), of the 2LQG model (red), and of the reduced model (3.16)–(3.17) (black circles). (*a*) Raw data for all models. (*b*) The mapping suggests plotting the data from the 2LQG and reduced models under the form $D_*/12$ versus $\sqrt{3}\,\mu_*$, which collapses the data of all models in the low-drag regime. The inset shows the same data compensated by a $-4/3$ power law. In each panel, the solid line represents the low-drag theoretical prediction (6.2) deduced from the mapping procedure.

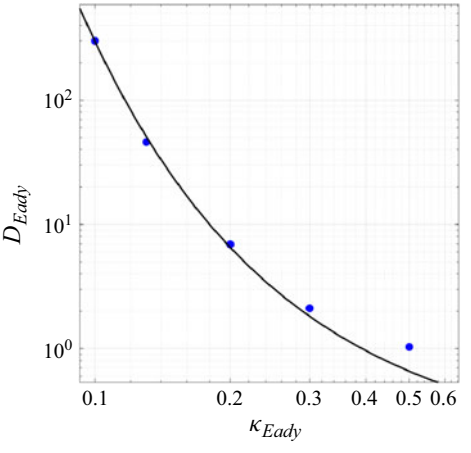


Figure 6. Effective diffusivity versus linear drag coefficient in the Eady model. Symbols are numerical simulations. The solid line is the low-drag theoretical prediction (6.2) deduced from the mapping procedure.

larger domain and a smaller hyperviscosity to better converge the diffusivity. The low-drag numerical data in figure 6 agree quantitatively with the theoretical prediction (6.2), which confirms that the mapping procedure is valid for both quadratic and linear drag.

7. Conclusion

Despite the different nature of the PV gradients involved in the Eady model and in the 2LQG model, the present study shows that the two systems share the exact same quantitative behaviour at large scale in the limit of weak bottom drag. Indeed, the two

https://doi.org/10.1017/jfm.2026.11943 Published online by Cambridge University Press

models asymptote to the same 'reduced' set of equations in this limit, i.e. when the integral scale of the flow is large compared to the Rossby deformation radius.

The heat transport of the QG Eady model is depth-invariant – a standard consequence of the Taylor–Bretherton relation, see e.g. Gallet *et al.* (2022) – with magnitude governed by an equivalent 2LQG model at low drag. As an illustration of this procedure, we derived a quantitative prediction for the low-drag asymptotic behaviour of the Eady diffusivity based on results from a vortex-gas scaling theory developed for the 2LQG model. It is interesting to note that the mapping leads to a quantitative match between the diffusivities of the Eady and 2LQG models up to values of the drag coefficient as high as $\mu_* \simeq 0.2$. That is, the mapping retains strong predictive skill beyond the conservative, asymptotically low-drag assumption under which it was derived, extending to regimes where the dimensionless diffusivity approaches unity. While the precise origin of this extended range of validity remains to be investigated, we notice that $\mu_* = 0.2$ lies in the acceptable range of values when modelling the Southern Ocean, corresponding to a dimensionless mixing length $\ell_* \simeq 7$ (as inferred from figure 3 in Gallet & Ferrari 2020). Assuming Rossby deformation radius 20 km in this region (Chelton *et al.* 1998) then leads to dimensional mixing length 140 km, much smaller than the lateral extent of the Antarctic Circumpolar Current.

Of course, the mapping between the two models holds for large-scale quantities only, such as the eddy diffusivity. By contrast, flow structures at scales smaller than the deformation radius strongly differ between the 2LQG and Eady models, as only the latter model presents the characteristics of SQG dynamics (e.g. fronts) near top and bottom (Capet *et al.* 2008; Lapeyre 2017).

A surprising aspect of the reduced set of equations is that while it captures large-scale 2LQG and Eady turbulence quantitatively, it does not capture linear baroclinic instability. This indicates that the properties of the turbulent flow are, in fact, somewhat disconnected from the instability mechanism. It would be worth investigating whether this property extends beyond the highly idealised 2LQG and Eady models, towards more realistic models of ocean mesoscale turbulence. If so, then one would naturally be led to reconsider parametrisations where the turbulent (Gent–McWilliams) diffusivity is assumed to be controlled by the Eady growth rate (Treguier *et al.* 1997; Visbeck *et al.* 1997).

In the QG Eady model, the vanishing-PV states come with an inversion relation that allows one to describe the evolution of the full 3-D system in terms of two 2-D fields only; see (2.1)–(2.3). If needed, the full 3-D fields are easily recovered from these 2-D fields using coupled SQG-like modes at top and bottom, as described in a slightly more general context in Callies *et al.* (2016). For horizontal wavenumbers comparable to the inverse deformation radius, the resulting modes have complicated vertical structure. This is the range of wavenumbers typically involved in the linear instability of the system. Luckily, an outcome of the present study is that the linear instability process is irrelevant in the equilibrated low-drag regime. Instead, most of the action takes place at scales much greater than the deformation radius. For such low wavenumbers, the vertical structure of the SQG-like modes extends over the whole depth of the domain, i.e. the boundary modes increasingly resemble interior modes. This may explain why we can successfully unveil a mapping between the Eady and 2LQG models in the low-drag equilibrated regime, while the same task remains challenging when focusing on the linear instability of the system (Rocha *et al.* 2016).

With the goal of narrowing the gap between the present highly idealised models and more realistic ocean flows, an interesting extension of this study would be to consider systems with a non-zero background PV gradient (Miller *et al.* 2024, 2025), resulting from latitudinal variations of the Coriolis parameter, sloping bottom topography (Deng & Wang 2024) or vertically dependent background shear and stratification (Smith & Marshall 2009;

https://doi.org/10.1017/jfm.2026.11943 Published online by Cambridge University Press

Meunier *et al.* 2023*a*). The first step in this direction could be a Charney model with weak planetary β (Charney 1947; Green 1960). In the weak-β regime, we derived a perturbative prediction for the vertical profile of the turbulent heat flux throughout the water column, up to an unknown prefactor set by the overall (depth-integrated) heat flux (Meunier *et al.* 2023*b*). An extension of the present mapping to $\beta \neq 0$ would complement the vertical profile with a prediction for the depth-integrated heat flux, based on the behaviour of a two-layer model with weak β (Arbic & Flierl 2004; Thompson & Young 2007; Chang & Held 2021; Gallet & Ferrari 2021).

Acknowledgements. We thank M. Lobo and two anonymous referees for their insightful comments that helped to improve the overall presentation of this work.

Funding. This research is supported by the European Research Council under grant agreement 101124590. This work has benefited from HPC resources from GENCI-IDRIS (Grant 2025-AD012A16265).

Declaration of interests. The authors report no conflict of interest.

Appendix A. Simulation parameters

The parameter values of all simulations are reported in table 2. As described in § 2, the dimensionless domain size is $L = \mathcal{L}/\lambda$ for the 2LQG model and the reduced model, while it is $L = \mathcal{L}f/(NH)$ for the Eady model. The spatial resolution along each horizontal direction is denoted by $\mathcal{N}$. The numerical simulations are performed using a GPU-based pseudo-spectral solver, the details of which can be found in Hadjerci & Gallet (2023). The domain size L and the dimensionless hyperviscosity ν are adjusted to ensure that the effective diffusivity $D_{*,Eady}$ is independent of these two parameters. The resolution $\mathcal{N}$ is chosen high enough for the hyperviscous cut-off wavenumber to remain well below

2LQG					Eady QG				
$\mathcal{N}$	$1/L$	μ_*	ν	D_*	$\mathcal{N}$	$1/L$	μ_{Eady}	ν	D_{Eady}
4096	0.0025	1.0×10^{-4}	7.9×10^{-2}	2.5×10^{5}					
2048	0.005	3.0×10^{-4}	7.8×10^{-2}	7.1×10^{4}	4096	0.005	3.0×10^{-4}	1.2×10^{-5}	3.2×10^{3}
2048	0.005	6.0×10^{-4}	7.8×10^{-2}	2.7×10^{4}	4096	0.01	6.0×10^{-4}	5.0×10^{-7}	1.4×10^{3}
1024	0.01	1.0×10^{-3}	7.8×10^{-2}	1.4×10^{4}	4096	0.01	1.0×10^{-3}	5.0×10^{-7}	6.7×10^{2}
1024	0.01	3.0×10^{-3}	7.8×10^{-2}	2.9×10^{3}	4096	0.01	3.0×10^{-3}	2.5×10^{-7}	1.3×10^{2}
2048	0.005	1.0×10^{-2}	7.8×10^{-2}	5.9×10^{2}	2048	0.02	1.0×10^{-2}	4.7×10^{-5}	2.47×10^{1}
1024	0.01	3.0×10^{-2}	7.8×10^{-2}	1.5×10^{2}	1024	0.04	3.0×10^{-2}	3.7×10^{-8}	6.8
1024	0.01	1.0×10^{-1}	7.8×10^{-2}	4.3×10^{1}	1024	0.04	1.0×10^{-1}	3.7×10^{-8}	2.3
512	0.02	3.0×10^{-1}	7.8×10^{-2}	1.7×10^{1}	1024	0.04	3.0×10^{-1}	3.7×10^{-8}	1.1

Reduced system

$\mathcal{N}$	$1/L$	μ_*	ν	D_*
4096	0.005	3.0×10^{-4}	8.0×10^{-4}	1.5×10^{4}
2048	0.01	1.0×10^{-3}	8.0×10^{-4}	3.0×10^{3}
2048	0.01	3.0×10^{-2}	8.0×10^{-4}	6.6×10^{2}
2048	0.01	1.0×10^{-2}	8.0×10^{-4}	1.1×10^{2}

Table 2. Simulation parameters for the 2LQG model, the QG Eady model and the reduced system, including the resolution $\mathcal{N}$ along each horizontal direction, the inverse dimensionless domain size $1/L$, the dimensionless drag coefficient $\mu_{*,Eady}$, the dimensionless hyperviscosity ν, and the measured dimensionless eddy diffusivity $D_{*,Eady}$ in statistically steady state.

https://doi.org/10.1017/jfm.2026.11943 Published online by Cambridge University Press

the maximum wavenumber $\mathcal{N}/3$, thereby preventing any spurious accumulation at small scale.

References

ARBIC, B.K. & FLIERL, G.R. 2004 Effects of mean flow direction on energy, isotropy, and coherence of baroclinically unstable beta-plane geostrophic turbulence. *J. Phys. Oceanogr.* **34** (1), 77–93.

CALLIES, J., FLIERL, G., FERRARI, R. & FOX-KEMPER, B. 2016 The role of mixed-layer instabilities in submesoscale turbulence. *J. Fluid Mech.* **788**, 5–41.

CAPET, X., KLEIN, P., HUA, B.L., LAPEYRE, G. & MCWILLIAMS, J.C. 2008 Surface kinetic energy transfer in surface quasi-geostrophic flows. *J. Fluid Mech.* **604**, 165–174.

CHANG, C.-Y. & HELD, I.M. 2019 The control of surface friction on the scales of baroclinic eddies in a homogeneous quasigeostrophic two-layer model. *J. Atmos. Sci.* **76** (6), 1627–1643.

CHANG, C.-Y. & HELD, I.M. 2021 The parameter dependence of eddy heat flux in a homogeneous quasigeostrophic two-layer model on a beta plane with quadratic friction. *J. Atmos. Sci.* **78** (1), 97–106.

CHARNEY, J.G. 1947 The dynamics of long waves in a baroclinic westerly current. *J. Atmos. Sci.* **4** (5), 136–162.

CHELTON, D.B., DESZOEKE, R.A., SCHLAX, M.G., EL NAGGAR, K. & SIWERTZ, N. 1998 Geographical variability of the first baroclinic Rossby radius of deformation. *J. Phys. Oceanogr.* **28** (3), 433–460.

CHEN, S.-N. 2023 Revisiting the baroclinic eddy scalings in two-layer, quasigeostrophic turbulence: effects of partial barotropization. *J. Phys. Oceanogr.* **53** (3), 891–913.

CONSTANTIN, P., MAJDA, A.J. & TABAK, E. 1994 Formation of strong fronts in the 2-D quasigeostrophic thermal active scalar. *Nonlinearity* **7** (6), 1495.

DENG, P. & WANG, Y. 2024 Distinct impacts of topographic versus planetary PV gradients on baroclinic turbulence. *J. Phys. Oceanogr.* **54** (10), 2205–2231.

EADY, E.T. 1949 Long waves and cyclone waves. *Tellus* **1** (3), 33–52.

FAUVE, S. & THUAL, O. 1990 Solitary waves generated by subcritical instabilities in dissipative systems. *Phys. Rev. Lett.* **64** (3), 282.

FLIERL, G.R. 1978 Models of vertical structure and the calibration of two-layer models. *Dyn. Atmos. Oceans* **2** (4), 341–381.

GALLET, B. 2024 Two-dimensional turbulence above topography: condensation transition and selection of minimum enstrophy solutions. *J. Fluid Mech.* **988**, A13.

GALLET, B. & FERRARI, R. 2020 The vortex gas scaling regime of baroclinic turbulence. *Proc. Natl Acad. Sci. USA* **117** (9), 4491–4497.

GALLET, B. & FERRARI, R. 2021 A quantitative scaling theory for meridional heat transport in planetary atmospheres and oceans. *AGU Adv.* **2** (3), e2020AV000362.

GALLET, B., MIQUEL, B., HADJERCI, G., BURNS, K.J., FLIERL, G.R. & FERRARI, R. 2022 Transport and emergent stratification in the equilibrated Eady model: the vortex-gas scaling regime. *J. Fluid Mech.* **948**, A31.

GALLET, B. & YOUNG, W.R. 2013 A two-dimensional vortex condensate at high Reynolds number. *J. Fluid Mech.* **715**, 359–388.

GREEN, J.S.A. 1960 A problem in baroclinic stability. *Q. J. R. Meteorol. Soc.* **86** (368), 237–251.

HADJERCI, G. & GALLET, B. 2023 Vortex core radius in baroclinic turbulence: implications for scaling predictions. *Phys. Rev. Fluids* **8** (9), 094501.

HELD, I.M., PIERREHUMBERT, R.T., GARNER, S.T. & SWANSON, K.L. 1995 Surface quasi-geostrophic dynamics. *J. Fluid Mech.* **282**, 1–20.

JULIEN, K. & KNOBLOCH, E. 2007 Reduced models for fluid flows with strong constraints. *J. Math. Phys.* **48** (6), 065405.

VAN KAN, A., FAVIER, B., JULIEN, K. & KNOBLOCH, E. 2022 Spontaneous suppression of inverse energy cascade in instability-driven 2-D turbulence. *J. Fluid Mech.* **952**, R4.

KOHL, M. & O'GORMAN, P.A. 2022 The diabatic Rossby vortex: growth rate, length scale, and the wave–vortex transition. *J. Atmos. Sci.* **79** (10), 2739–2755.

LACASCE, J.H. 2012 Surface quasigeostrophic solutions and baroclinic modes with exponential stratification. *J. Phys. Oceanogr.* **42** (4), 569–580.

LAPEYRE, G. 2009 What vertical mode does the altimeter reflect? On the decomposition in baroclinic modes and on a surface-trapped mode. *J. Phys. Oceanogr.* **39** (11), 2857–2874.

LAPEYRE, G. 2017 Surface quasi-geostrophy. *Fluids* **2** (1), 7.

LARICHEV, V.D. & HELD, I.M. 1995 Eddy amplitudes and fluxes in a homogeneous model of fully developed baroclinic instability. *J. Phys. Oceanogr.* **25** (10), 2285–2297.

https://doi.org/10.1017/jfm.2026.11943 Published online by Cambridge University Press

LOBO, M. 2025 Baroclinic energy cycles in two-layer quasi-geostrophic turbulence. *J. Fluid Mech.* **1023**, A2.
LOBO, M. & GRIFFIES, S.M. 2026 *Two-Layer Quasi-Geostrophic Waves and Turbulence over a Meridionally Sloping Bottom with Linear Bottom Drag*. Authorea Preprints.
MEUNIER, J. & GALLET, B. 2025 Effective transport by 2D turbulence: vortex-gas theory vs scale-invariant inverse cascade. *Phys. Rev. Lett.* **134**, 074101.
MEUNIER, J., MIQUEL, B. & GALLET, B. 2023*a* A direct derivation of the Gent–McWilliams/Redi diffusion tensor from quasi-geostrophic dynamics. *J. Fluid Mech.* **963**, A22.
MEUNIER, J., MIQUEL, B. & GALLET, B. 2023*b* Vertical structure of buoyancy transport by ocean baroclinic turbulence. *Geophys. Res. Lett.* **50** (17), e2023GL103948.
MILLER, L., DEREMBLE, B. & VENAILLE, A. 2024 Gyre turbulence: anomalous dissipation in a two-dimensional ocean model. *Phys. Rev. Fluids* **9** (5), L051801.
MILLER, L., DEREMBLE, B. & VENAILLE, A. 2025 The impact of stratification on surface-intensified eastward jets in turbulent gyres. *J. Phys. Oceanogr.* **55** (9), 1535–1551.
PEDLOSKY, J. 2013 *Geophysical Fluid Dynamics*. Springer Science & Business Media.
PHILLIPS, N.A. 1954 Energy transformations and meridional circulations associated with simple baroclinic waves in a two-level, quasi-geostrophic model. *Tellus* **6** (3), 274–286.
PUDIG, M.P. & SMITH, K.S. 2025 Baroclinic turbulence above rough topography: the vortex gas and topographic turbulence regimes. *J. Phys. Oceanogr.* **55** (5), 611–630.
ROCHA, C.B., YOUNG, W.R. & GROOMS, I. 2016 On Galerkin approximations of the surface active quasigeostrophic equations. *J. Phys. Oceanogr.* **46** (1), 125–139.
SALMON, R. 1978 Two-layer quasi-geostrophic turbulence in a simple special case. *Geophys. Astrophys. Fluid Dyn.* **10** (1), 25–52.
SALMON, R. 1980 Baroclinic instability and geostrophic turbulence. *Geophys. Astrophys. Fluid Dyn.* **15** (1), 167–211.
SALMON, R. 1998 *Lectures on Geophysical Fluid Dynamics*. Oxford University Press.
SCOTT, R.B. & FURNIVAL, D.G. 2012 Assessment of traditional and new eigenfunction bases applied to extrapolation of surface geostrophic current time series to below the surface in an idealized primitive equation simulation. *J. Phys. Oceanogr.* **42** (1), 165–178.
SCOTT, R.K. & DRITSCHEL, D.G. 2014 Numerical simulation of a self-similar cascade of filament instabilities in the surface quasigeostrophic system. *Phys. Rev. Lett.* **112** (14), 144505.
SMITH, K.S. & MARSHALL, J. 2009 Evidence for enhanced eddy mixing at middepth in the Southern Ocean. *J. Phys. Oceanogr.* **39** (1), 50–69.
SMITH, K.S. & VANNESTE, J. 2013 A surface-aware projection basis for quasigeostrophic flow. *J. Phys. Oceanogr.* **43** (3), 548–562.
SPRAGUE, M., JULIEN, K., KNOBLOCH, E. & WERNE, J. 2006 Numerical simulation of an asymptotically reduced system for rotationally constrained convection. *J. Fluid Mech.* **551**, 141–174.
STERL, M.F., PALÓCZY, A., GROESKAMP, S., BAATSEN, M.L.J., LACASCE, J.H. & ISACHSEN, P.E. 2025 The joint effects of planetary β, topography and friction on baroclinic instability in a two-layer quasi-geostrophic model. *J. Fluid Mech.* **1012**, A1.
THOMPSON, A.F. & YOUNG, W.R. 2006 Scaling baroclinic eddy fluxes: vortices and energy balance. *J. Phys. Oceanogr.* **36** (4), 720–738.
THOMPSON, A.F. & YOUNG, W.R. 2007 Two-layer baroclinic eddy heat fluxes: zonal flows and energy balance. *J. Atmos. Sci.* **64** (9), 3214–3231.
TREGUIER, A.M., HELD, I.M. & LARICHEV, V.D. 1997 Parameterization of quasigeostrophic eddies in primitive equation ocean models. *J. Phys. Oceanogr.* **27** (4), 567–580.
TULLOCH, R. & SMITH, K.S. 2009 Quasigeostrophic turbulence with explicit surface dynamics: application to the atmospheric energy spectrum. *J. Atmos. Sci.* **66** (2), 450–467.
VALADE, N., BEC, J. & THALABARD, S. 2025 Surface quasigeostrophic turbulence: the refined study of an active scalar. *J. Fluid Mech.* **1021**, A17.
VALLIS, G.K. 2017 *Atmospheric and Oceanic Fluid Dynamics*. Cambridge University Press.
VISBECK, M., MARSHALL, J., HAINE, T. & SPALL, M. 1997 Specification of eddy transfer coefficients in coarse-resolution ocean circulation models. *J. Phys. Oceanogr.* **27** (3), 381–402.
YASSIN, H. & GRIFFIES, S.M. 2022 On the discrete normal modes of quasigeostrophic theory. *J. Phys. Oceanogr.* **52** (2), 243–259.

https://doi.org/10.1017/jfm.2026.11943 Published online by Cambridge University Press